Propulsion and Energy Forum
July 27-29, 2015, Orlando, FL
13th International Energy Conversion Engineering Conference

Effects of Magnetohydrodynamic Energy Generation on Planetary Entry Vehicle Flight Dynamics

Hisham K. Ali [1] and Robert D. Braun[2]
Space Systems Design Laboratory, Georgia Institute of Technology
270 Ferst Drive, Atlanta, GA 30331

Proposed missions such as a Mars sample return mission and a human mission to Mars require landed payload masses in excess of any previous Mars mission. Due to their large mass and high complexity, these missions present numerous engineering challenges to existing technologies, particularly those of the entry, descent, and landing system. To overcome these challenges, new technologies must be developed, and existing technologies advanced. For this study, the performance of magnetohydrodynamic energy generation system for drag augmentation and flow control during Mars entry is investigated. Results include computed deceleration and trajectory influences caused by magnetohydrodynamic interaction as a function of vehicle configuration, entry velocity, applied magnetic field strength, and alkali seed particle mass fraction.

Nomenclature

$\boldsymbol{A}$	=	vehicle characteristic area
$\boldsymbol{B}$	=	magnetic field strength
$\overline{\boldsymbol{B}}$	=	magnetic field vector
$\boldsymbol{C}$	=	lorentz force constant
$\boldsymbol{C_D}$	=	vehicle drag coefficient
$\boldsymbol{D}$	=	vehicle diameter
$\overline{\boldsymbol{E}}$	=	electric field vector
$\boldsymbol{e}$	=	elementary charge
$\boldsymbol{F_{MHD}}$	=	Lorentz force magnitude
$\overline{\boldsymbol{F}}_{\boldsymbol{MHD}}$	=	Lorentz force vector
$\boldsymbol{n_e}$	=	electron number density
$\boldsymbol{n}$	=	post shock number density
$\boldsymbol{m}$	=	vehicle mass
$\boldsymbol{m_e}$	=	electron mass
$\forall$	=	shock layer volume
$\bar{\boldsymbol{r}}$	=	radial distance between vehicle and Mars center of mass
$\boldsymbol{u_\infty}$	=	vehicle velocity
$\boldsymbol{\beta}$	=	ballistic coefficient
$\boldsymbol{\Delta}$	=	shock standoff distance
$\boldsymbol{\mu_{Mars}}$	=	mars gravitational parameter
$\boldsymbol{\rho_\infty}$	=	atmospheric density
$\boldsymbol{\sigma}$	=	electrical conductivity
$\boldsymbol{\nu_{e,s}^m}$	=	electron species collision frequency

[1] Graduate Research Assistant, Aerospace Engineering, AIAA Member
[2] David and Andrew Lewis Professor of Space Technology, Aerospace Engineering, AIAA Fellow

I. Introduction and Motivation

Previous Mars missions have relied primarily on Viking era technology for entry, descent, and landing. [1] The limit of this technology is being reached, with the Mars Science Laboratory (MSL) landing in 2012 illustrating the difficulty in high mass Martian landings with current technology.

Due to ever higher mass requirements for future Mars missions such as a Mars Sample Return or Mars Human Mission, significant technology development is required. A typical Mars probe that arrives after completing an interplanetary transfer carries an enormous amount of kinetic energy that must be dissipated safely. Previous Mars missions have shown that the majority of an entry vehicle's kinetic energy is dissipated during the hypersonic phase of entry, about 92.5% in the case of Mars Pathfinder.[2] During this hypersonic phase of entry, there exists a highly heated, partially ionized flow around the vehicle in the shock layer. The free electrons in the shock layer can be harnessed to create a sustained, usable electric current via in-situ magnetohydrodynamic power generation, reclaiming some of the vehicle's dissipated kinetic energy.[3]

In-situ magnetohydrodynamic power generation systems for planetary entry inherently contain a mechanism for facilitating magnetohydrodynamic flow interaction. Magnetohydrodynamic flow interaction for high speed aerospace applications has been studied since the dawn of the space race, with early theoretical studies dating back to the late fifties and early sixties.[4]–[6] These studies focused primarily on the flow control applications possible with magnetohydrodynamic interaction for purposes such as drag and peak heating modulation. At the time, such magnetohydrodynamic flow control systems were limited by available technologies, as the coils needed to produce the necessary magnetic field were mass prohibitive and subject to intense joule heat dissipation of their own. Since that time, however, dramatic advances in superconductivity and magnetic field generation have been made, and in conjunction with a pressing need to reduce interplanetary launch masses, warrants additional investigation of the topic.

More recent studies use full-field numerical techniques made feasible by ever increasing computational capabilities, and have considered the effects on vehicle flight dynamics and heat transfer, primarily dealing with Earth entry[7], [8], although some studies have also been made for Mars entry[9], [10]. All of these numerical studies found the potential for reduced heat transfer to the vehicle as well as the potential for increased drag due to observed increases in the shock standoff distance. Indeed, these phenomena were also observed in the limited experimental studies conducted on the subject thus far[11], [12].

However, most previous studies considered Earth entry, and where they did not, examined a particular vehicle configuration in detail. It would be of great benefit to extend these analysis techniques to a system level study for Mars entry incorporating a variety of entry vehicles, alkali metal seed mass fraction, and applied magnetic field strengths. The contributions presented in the sections that follow move towards the realization of these goals. The vehicles under study include previously flown configurations such as the Mars Pathfinder entry vehicle, as well as future concepts such as a Mars Human Mission class entry vehicle. Non-lifting entry trajectories are simulated for each vehicle and applied magnetic field strength, and an assessment is made of the impact of the applied magnetic field and augmented drag on the trajectory. Results include altitude vs. velocity plots, deceleration vs. altitude plots, and tabulated peak decelerations. Following the presentation and discussion of the results, the observations are summarized and conclusions drawn. Finally, recommendations for future work on the subject are made.

II. Relevant Background and Theoretical Approach

A. Determining the Influence of Magnetohydrodynamic Flow Interaction

For the ionized, hypersonic flow-field around a blunt-body entry vehicle with an applied magnetic field, there will exist an additional body force on the fluid due the magnetohydrodynamic flow interaction, called the Lorentz force. This force, denoted as $\overline{\boldsymbol{F}}_{\boldsymbol{MHD}}$, acts on the entry vehicle through the magnetic field, and is expressed as equation 1 below[8]

$$\overline{\boldsymbol{F}}_{\boldsymbol{MHD}} = \iiint \bar{\boldsymbol{J}} \times \overline{\boldsymbol{B}} \boldsymbol{d}\forall \tag{1}$$

where $\bar{\mathbf{J}}$ represents the electric current density vector, and $\overline{\mathbf{B}}$ represents the applied magnetic field vector. The electrical current density can be determined through an application of Ohm's law, given below as equation 2.

$$\bar{\boldsymbol{J}} = \boldsymbol{\sigma}(\overline{\boldsymbol{E}} + \overline{\boldsymbol{u}} \times \overline{\boldsymbol{B}}) \tag{2}$$

where $\boldsymbol{\sigma}$ is the local electrical conductivity. In the manner of reference [8], the Hall effect is neglected in equation 2 by assuming that the entry vehicle walls are non-conductive. Furthermore, in conjunction with an assumed axisymmetric magnetic field, there is no induced electric field and the current density vector will only have an azimuthal component. In further assuming that all flow properties in the shock layer, such as electrical conductivity, velocity, and density are constant, the following equation is obtained for the axial Lorentz force acting on the vehicle due to magnetohydrodynamic flow interaction.

$$\boldsymbol{F}_{\boldsymbol{MHD}} = \boldsymbol{\sigma u}_{\boldsymbol{post-shock}} \boldsymbol{B}^{\boldsymbol{2}} \forall_{\boldsymbol{shock-layer}} \tag{3}$$

where B is the magnitude of the applied magnetic field, also assumed constant throughout the shock layer and $\forall_{\boldsymbol{shock-layer}}$ is the volume of the shock layer, with the electrical conductivity and thus the current density assumed to be zero everywhere else in the flow.

The post shock velocity is determined by applying conservation of mass across a steady, one-dimensional shock wave, and is given below as follows

$$\boldsymbol{u}_{\boldsymbol{post-shock}} = \frac{\boldsymbol{\rho}_{\infty}}{\boldsymbol{\rho}_{\boldsymbol{post-shock}}} \boldsymbol{u}_{\infty} \tag{4}$$

where $\boldsymbol{\rho}_{\infty}$ represents the free-stream density, $\boldsymbol{\rho}_{\boldsymbol{post-shock}}$ represents the shock layer density, and $\boldsymbol{u}_{\infty}$ represents the free-stream velocity.

The shock layer volume is approximated as the product of the shock separation distance, $\boldsymbol{\Delta}$, and the projected vehicle area, $\boldsymbol{A}$, and is given below as equation 5.

$$\forall_{\boldsymbol{shock-layer}} = \boldsymbol{\Delta A} \tag{5}$$

The shock separation distance for a axisymmetric blunt body is strong function of the shock density ratio [13], and is given below as equation 6.

$$\boldsymbol{\Delta} \propto \frac{\boldsymbol{\rho}_{\infty}}{\boldsymbol{\rho}_{\boldsymbol{post-shock}}} \boldsymbol{D} \tag{6}$$

Where $\boldsymbol{D}$ is the vehicle diameter. Since the projected area is itself a function of diameter, equation 5 can be rewritten as follows

$$\forall_{\boldsymbol{shock-layer}} = \propto \frac{\boldsymbol{\rho}_{\infty}}{\boldsymbol{\rho}_{\boldsymbol{post-shock}}} \boldsymbol{D}^{\boldsymbol{3}} \tag{7}$$

Combining equations 4 and 7 and substituting into equation 3 gives the following relationship for the additional axial force caused by magnetohydrodynamic flow interaction

$$\boldsymbol{F}_{\boldsymbol{MHD}} = \boldsymbol{C\sigma u}_{\infty} \boldsymbol{B}^{\boldsymbol{2}} \left(\frac{\boldsymbol{\rho}_{\infty}}{\boldsymbol{\rho}_{\boldsymbol{post-shock}}} \right)^{\boldsymbol{2}} \boldsymbol{D}^{\boldsymbol{3}} \tag{8}$$

where $\boldsymbol{C}$ is a constant of proportionality, determined from a survey of prior results for MHD drag and is function of the vehicle, flow field, and magnetic field geometries. For the vehicle configurations under consideration in this analysis, $\boldsymbol{C}$ had a value of 0.0564.

The scalar electrical conductivity behind the shock is based on the electron number density and electron mobility, determined by the frequency of all electron-ion and electron-neutral collisions. The resulting expression is given below as equation 9.[8]

$$\sigma = \frac{n_e e^2}{m_e \sum_{s \neq e} \nu_{e,s}^m} \tag{9}$$

where n_e is the electron number density, e is the elementary charge, m_e is the mass of an electron, and $\nu_{e,s}^m$ is the collision frequency of electrons with a chemical species s. True calculation of the collision frequencies involves knowledge of the temperatures for each species, the collision cross sections, as well as the number density of each species. For simplicity and computational expediency; however, the electrical conductivity model for the Martian atmosphere suggested in [9] is used, given below as equation 10.

$$\sigma = 2.7x10^5 \frac{n_e}{n} \quad , \quad \left(\frac{1}{\Omega m}\right) \tag{10}$$

where n is the post shock overall number density and $\frac{1}{\Omega m}$ is the unit of electrical conductivity.

B. Entry Trajectory Dynamics Simulation

During atmospheric entry, an entry vehicle to which a magnetic field is applied is subject to gravitational, aerodynamic, and magnetohydrodynamic forces. The resulting equation of motion for the entry vehicle relative to Martian center of mass is given below as equation 11.

$$\ddot{\bar{r}} = -\frac{\mu_{Mars}}{(\bar{r} \cdot \bar{r})^{\frac{3}{2}}} \bar{r} - \left(\frac{\rho_\infty {u_\infty}^2}{2\beta} + \frac{F_{MHD}}{m}\right)\hat{\dot{\bar{r}}} \tag{11}$$

where μ_{Mars} is the Martian gravitational parameter, and β is the vehicle ballistic coefficient, defined below as follows

$$\beta = \frac{m}{C_D A} \tag{12}$$

where m is the entry vehicle mass, C_D is the entry vehicle drag coefficient, and A is the entry vehicle area.

During the simulation, the altitude and free-stream velocity are determined from the position and velocity state vectors. The altitude specifies the ambient atmospheric temperature, pressure, and density necessary to compute the post shock solution and vehicle dynamics. The chemical composition used throughout the simulation is that of the Martian atmosphere, which is relatively constant with altitude and is given below as Table 1.[14]

Table 1 Martian Atmospheric Composition[14]

Constituent	Relative Abundance
CO_2	96.0%
Ar	1.9%
N_2	1.9%
O_2	0.14%
CO	0.06%

The free-stream chemical composition in Table 1 can be altered by considering the addition of a small mass fraction of easily ionizable alkali metal seed such as potassium into the shock layer. It was found in [9] that the post-shock electron number density and thus the electrical conductivity and magnetohydrodynamic interaction effect are significantly enhanced at even potassium seed mass fractions of less than 1%. As such, variable free-stream chemical compositions are considered for potassium seed mass fractions between 0% and 1%.

The selected potassium seeding mass fraction, together with the ambient atmospheric temperature and pressure as well as the free-stream velocity, fully specify the solution to the one-dimensional equilibrium shock problem with chemistry. Post shock species include: Ar, C, N, O, C_2, N_2, O_2, CN, CO, NO, CO_2, NCO, Ar^+, C^+, C_2^+, N^+, N_2^+, O^+, O_2^+, CN^+, CO^+, NO^+, and e^-. In the case of seeding, there will also be K+ present in the post-shock species. The

ambient atmospheric pressure and temperature are themselves functions of altitude. Thus at each point in the trajectory simulation, the post shock properties and species composition needed in the computation of the magnetohydrodynamic interaction force can be calculated as a function of altitude and free-stream velocity.

The equations of motion presented as equation 11 are then solved numerically giving the resultant trajectory subject to magnetohydrodynamic flow interaction.

III. Methodology and Experimental Design

A. Calculation of Post shock Properties as a Function of Altitude and Velocity

The aforementioned trajectory study is implemented in MATLAB. As mentioned earlier, the ambient atmospheric temperature and pressure can be represented as simple functions of altitude, with temperature following a linear and pressure following an exponential relationship with altitude. The Martian atmospheric composition is taken from that reported by reference [14], and the relative chemical abundances are assumed to remain constant with altitude. From the previous section, it is found that the altitude, freestream velocity, and atmospheric chemical composition fully specify the solution to the equilibrium one-dimensional shock problem. Alkali metal seeding with potassium is accounted for by adding the appropriate mass fraction of potassium to the initial chemical composition in the simulation.

Once a seed mass fraction is selected, the post shock state is solved using NASA's Chemical Equilibrium with Applications Code[15] for a range of altitudes between 0 and 100 km and a range of velocities from 2500 to 7500 m/s. The post shock properties at each grid point are stored for efficient computation of these chemical properties at a later point. These properties are the electron number density, shock density ratio, post shock velocity, ionization fraction, electrical conductivity, temperature, and molecular composition. Post shock properties of particular interest to this simulation are the density ratio across the shock and electrical conductivity. Contour plots of these parameters at 0% and 1% mass fraction potassium seed are given below as Figures 1 through 4.

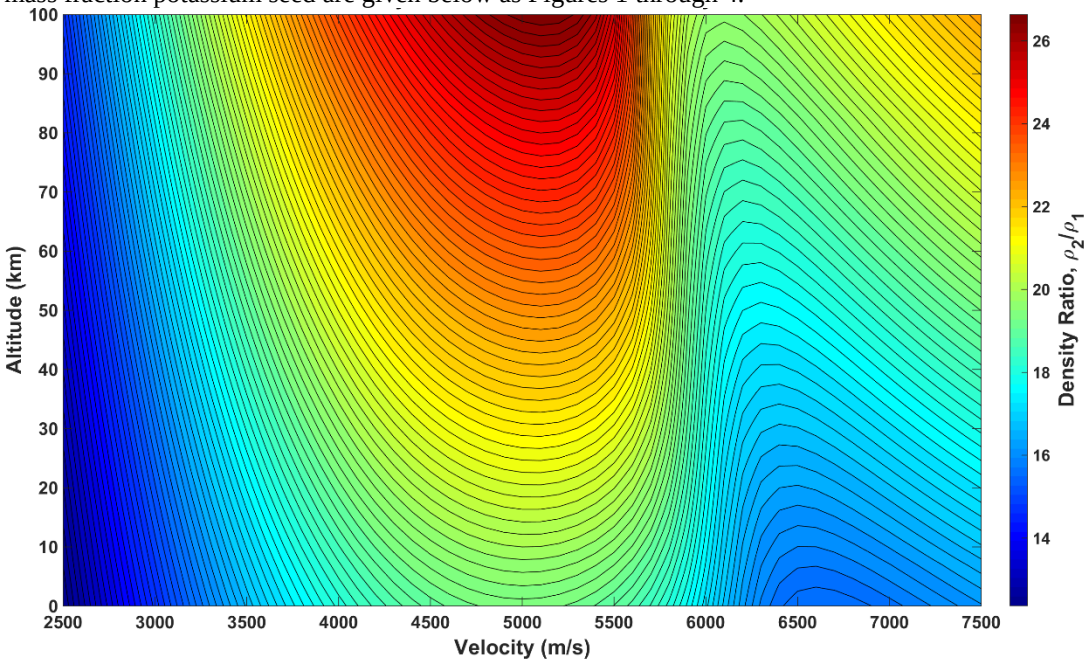

Figure 1. 0% K seed shock density ratio as a function of altitude and freestream velocity.

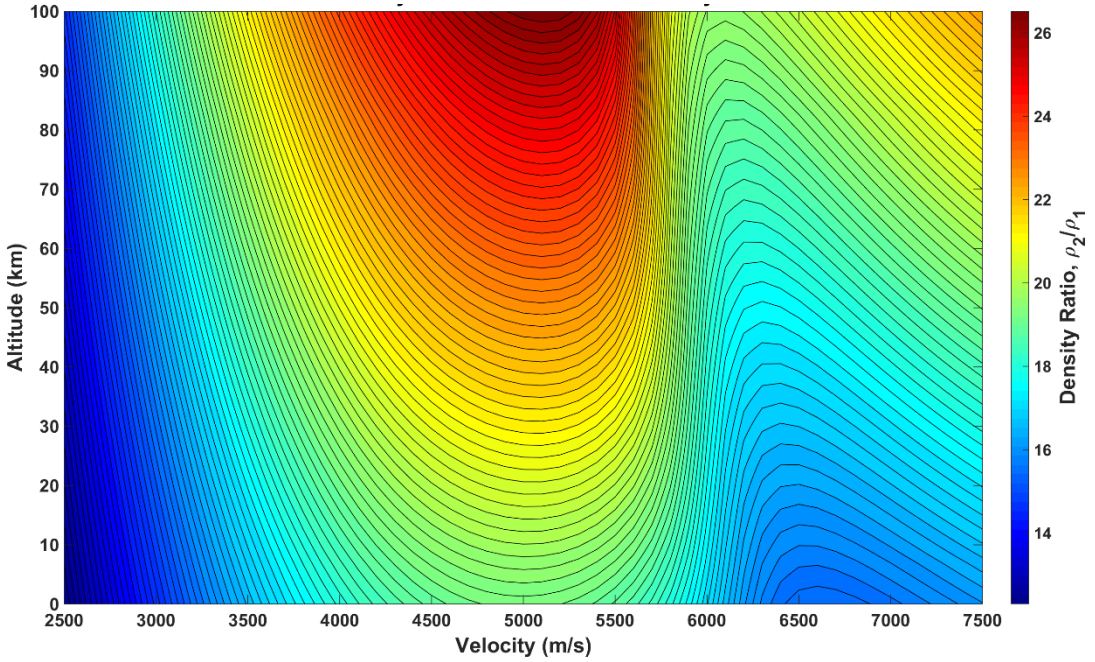

Figure 2. 1% K seed shock density ratio as a function of altitude and freestream velocity.

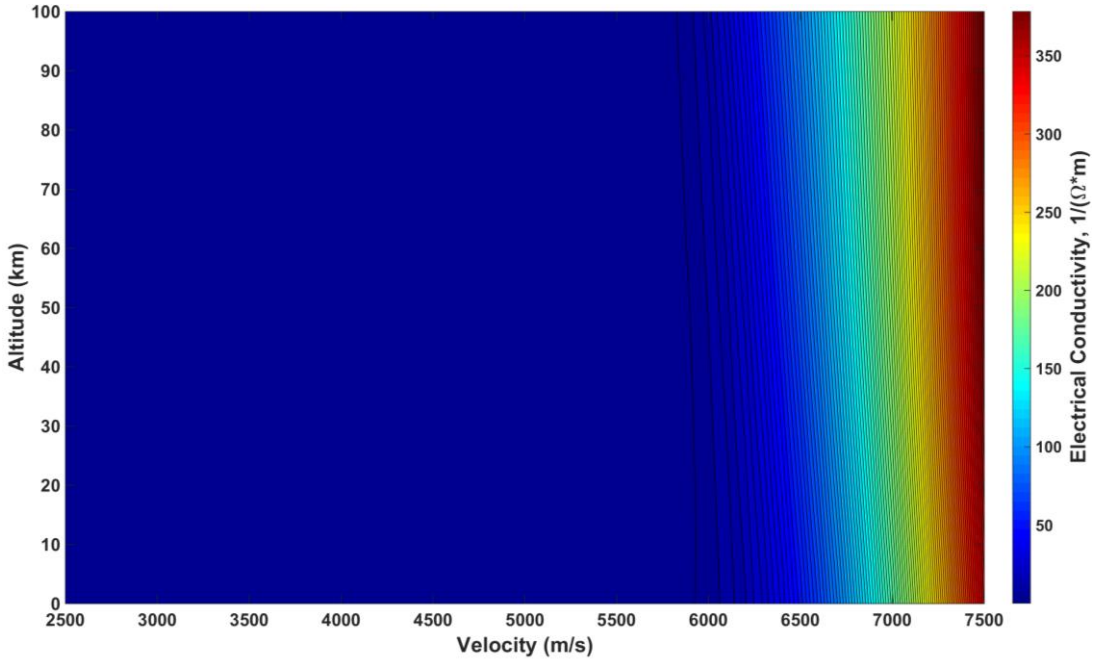

Figure 3. 0% K seed post shock electrical conductivity as a function of altitude and freestream velocity.

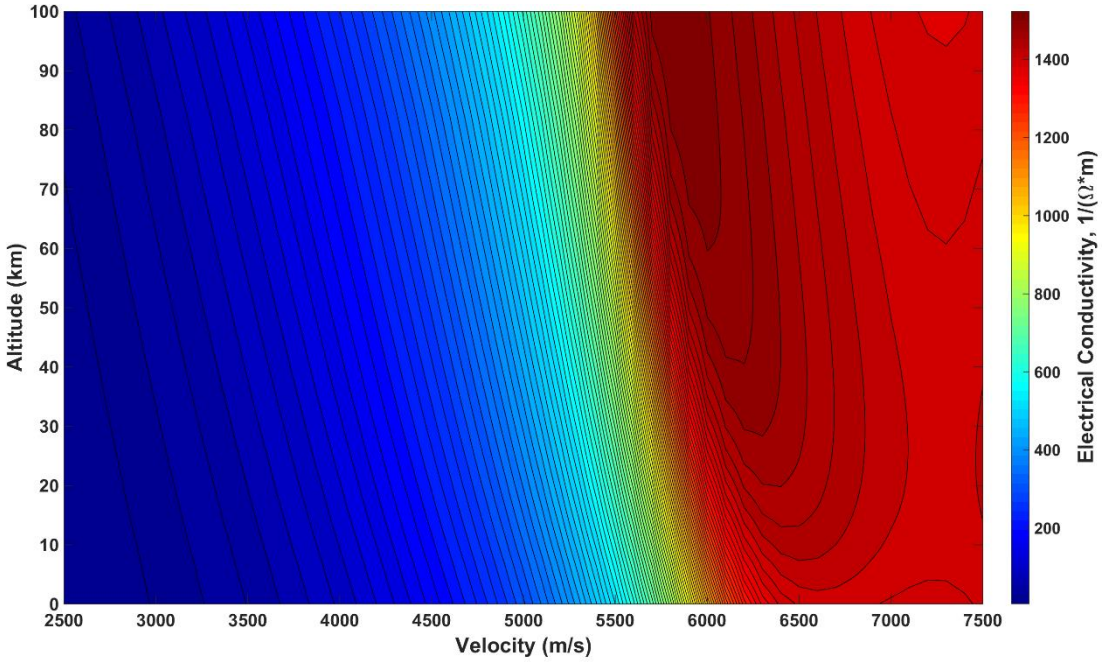

Figure 4. 1% K seed post shock electrical conductivity as a function of altitude and freestream velocity.

A comparison of Figures 1 and 2 reveals that the addition of alkali metal seed does not significantly alter the density ratio across the shock. As expected, however, the electrical conductivity changes significantly with the addition of the potassium seed, with substantially higher electrical conductivity across the simulation domain for the 1% mass fraction potassium seed case.

B. Trajectory Simulation with Magnetohydrodynamic Flow Control

The equations of motion are numerically integrated in MATLAB. Given the initial conditions, vehicle parameters, and applied magnetic field magnitude, the position and velocity states of the entry vehicle subject to gravity, aerodynamic, and magnetohydrodynamic interaction forces are computed. The simulation is terminated once the vehicle reaches the surface. In addition, a seeding mass fraction is specified, allowing for calculation of the post-shock properties for determination of the magnetohydrodynamic interaction force using the technique described in the previous section. Vehicle properties for the systems considered are given below as Table 2.

Table 2 Test Vehicle Configurations

Vehicle	Mass (kg)	C_D	A (m^2)	β (kg/m^2)
Mars Pathfinder	**582**	**1.68**	**5.52**	**63.1**
Mars Science Lab	**3151**	**1.68**	**16.6**	**112.9**
Moses Test Vehicle[4]	**1000**	**0.4**	**7.00**	**357.1**
Mars Human Mission	**100,000**	**1.68**	**78.5**	**757.9**

The initial conditions for all four vehicles were taken as an altitude of 100km and an initial flight path angle of 11 degrees. A summary of the trajectories that result from these initial conditions when no magnetic field is applied is presented below as Table 3.

Table 3 Initial Conditions for Each Test Vehicle Configuration at 100 km Altitude, No B-Field Applied

Vehicle	7 km/s Entry Velocity	
	$\gamma_{entry}(^{o})$	Time in Atm(s)
Mars Pathfinder	**-11.00**	**242**
Mars Science Lab	**-11.00**	**223**
Moses Test Vehicle	**-11.00**	**204**
Mars Human Mission	**-11.00**	**215**

Once the potassium seed mass fraction, vehicle configuration, and initial conditions are specified, the addition of the applied magnetic field gives the resultant trajectory and associated results. Sample results for the Mars Pathfinder Entry system with 1% mass fraction potassium seed are given below as Figures 5 and 6.

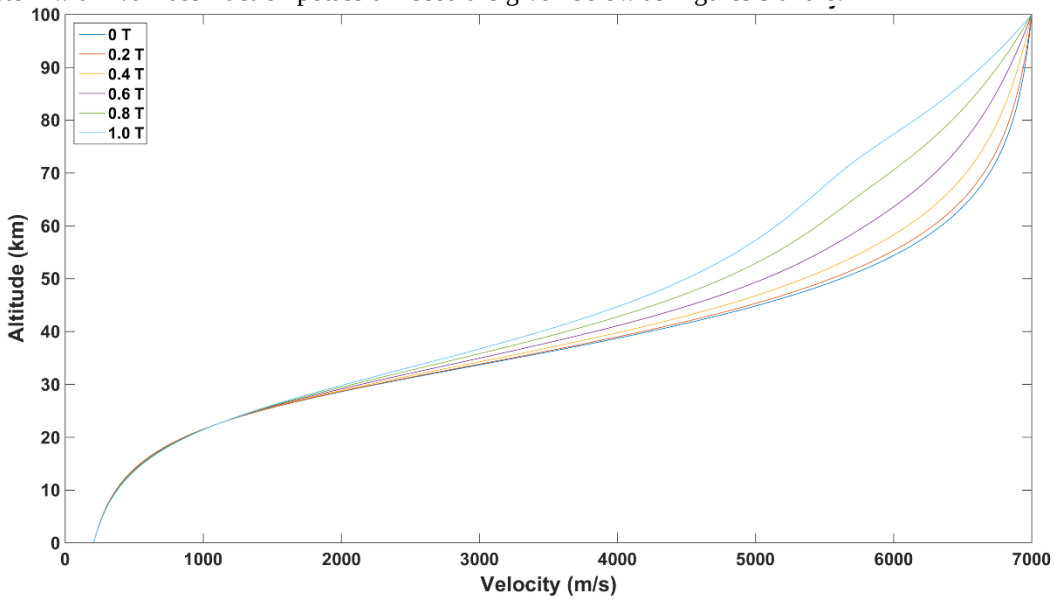

Figure 5. 1% K seed Mars Pathfinder altitude vs. velocity curves for various B field magnitudes.

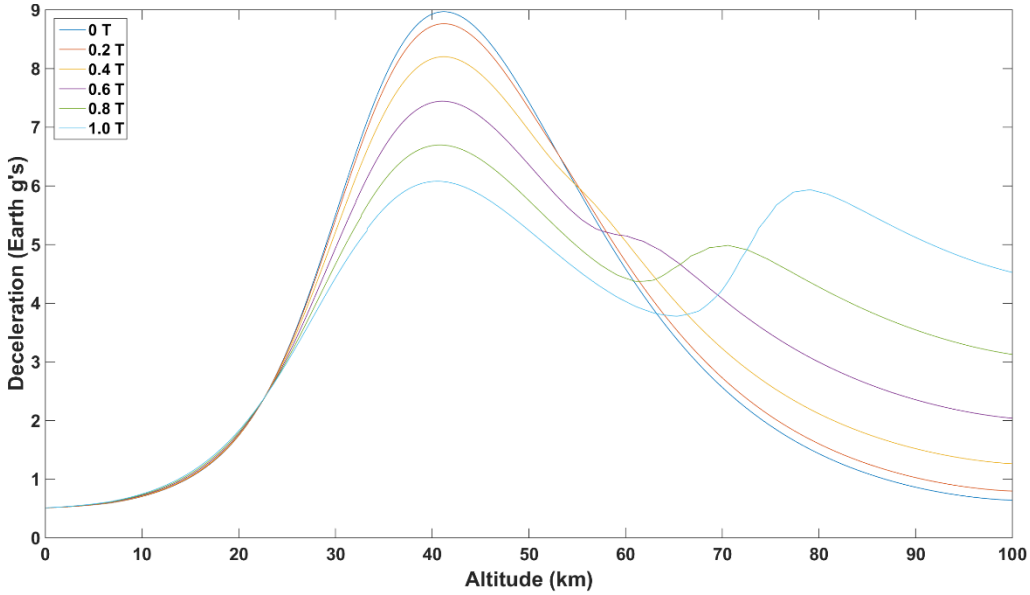

Figure 6. 1% K seed Mars Pathfinder total deceleration vs. altitude for various B field magnitudes.

C. Parameter Study

Using the analysis techniques described above, a parameter study was conducted. There existed a total of four input parameters with the following levels: 5 potassium seed mass fractions, 4 vehicle configurations, 1 trajectory initial condition, and 6 applied magnetic field magnitudes, summarized below as Table 4. The result was 120 unique parameter combinations. For each parameter combination, the resultant trajectory, deceleration profile, and electrical conductivity profile were stored and plotted. The results of this study are presented in the following section.

Table 4 Parameter Study Names and Values

Seeding Levels	Vehicle Configurations	Trajectory Types	Applied B Field Mag.
Unseeded	Mars Pathfinder	7km/s Direct Entry	0.0 T
0.25% K Mass Fraction	Mars Science Lab		0.2 T
0.50% K Mass Fraction	Moses Test Vehicle		0.4 T
0.75% K Mass Fraction	Mars Human Mission		0.6 T
1.00% K Mass Fraction			0.8 T
			1.0 T

IV. Results and Discussion

A. Altitude vs. Velocity: Influence of Magnetohydrodynamic Energy Generation on Trajectory

The altitude vs velocity trajectory profiles for each vehicle configuration are presented below for the unseeded and 1% mass fraction potassium seed case as Figures 7 – 14.

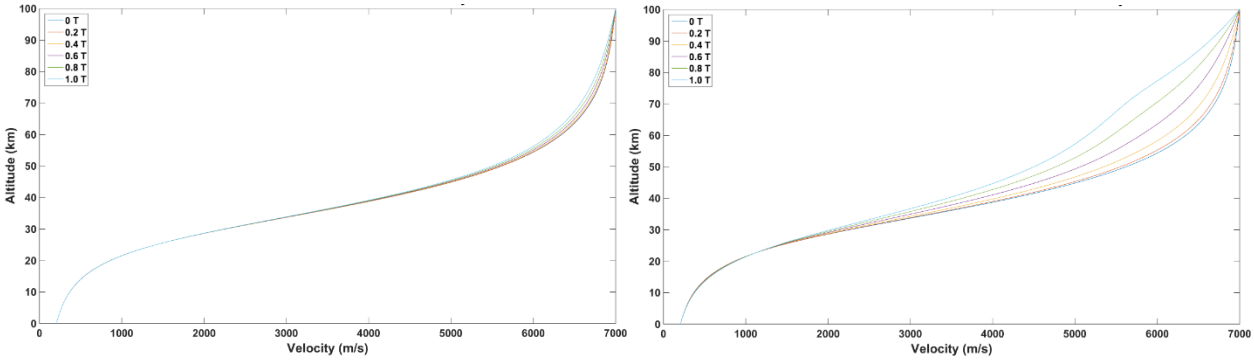

Figures 7 (left) and 8 (right). Unseeded (left) and 1% K seed (right) Mars Pathfinder altitude vs. velocity curves for various applied B fields.

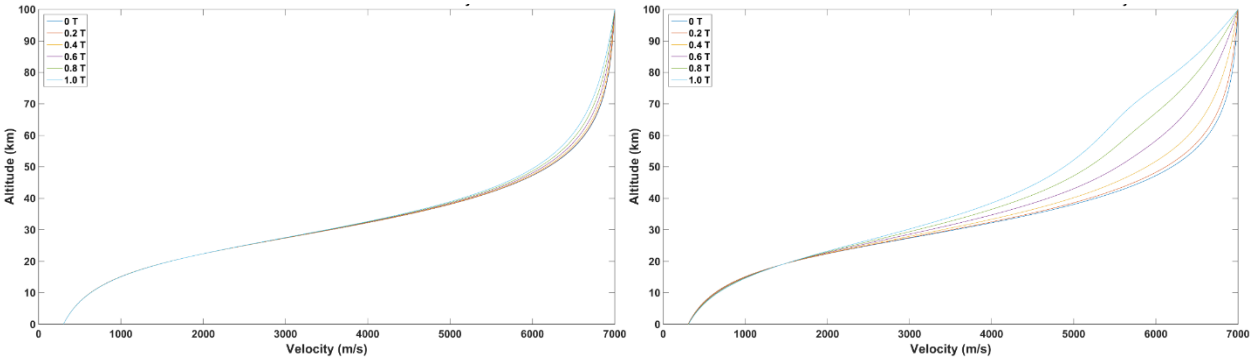

Figures 9 (left) and 10 (right). Unseeded (left) and 1% K seed (right) Mars Science Lab altitude vs. velocity curves for various applied B fields.

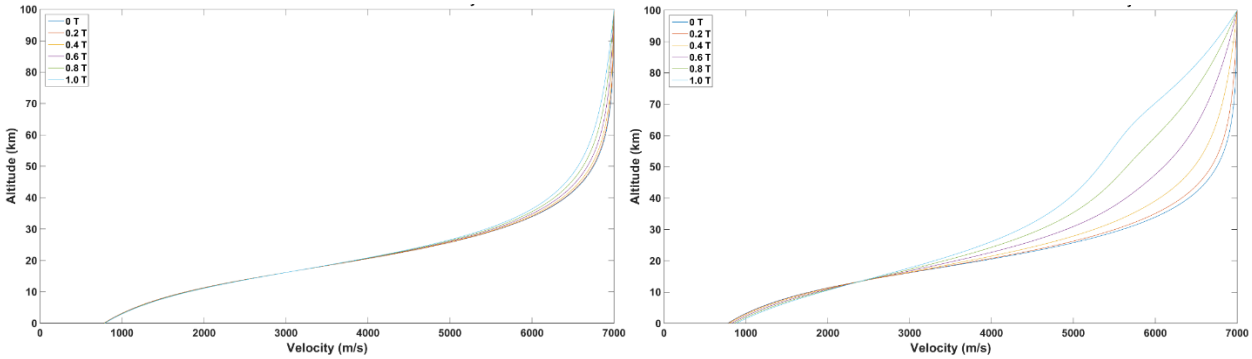

Figures 11 (left) and 12 (right). Unseeded (left) and 1% K seed (right) Moses Test Vehicle altitude vs. velocity curves for various applied B fields.

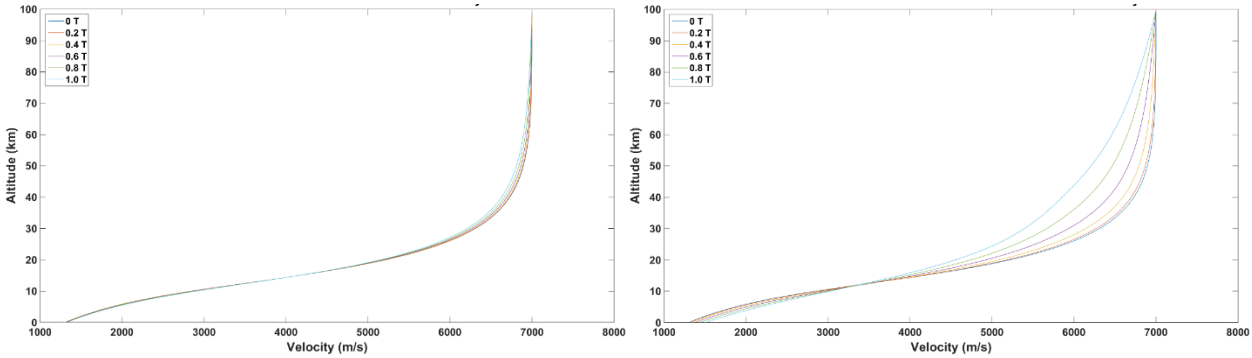

Figures 13 (left) and 14 (right). Unseeded (left) and 1% K seed (right) Mars Human Mission altitude vs. velocity curves for various applied B fields

The results presented show that for all vehicle configurations and in both the unseeded and 1% K seeded cases, the trajectory is influenced by magnetohydrodynamic flow interaction. It is also evident that the influence of magnetohydrodynamic flow interaction on the vehicle altitude history is much more significant in the 1% K seeded case as opposed to the unseeded case, as is expected due to the variance in electrical conductivity shown by Figures 3 and 4. Moreover, it appears that the larger the ballistic coefficient is relative to the mass of the entry vehicle, the larger the effect on vehicle trajectory. The most extreme case, the Moses Test Vehicle, with a mass of 1000kg and a ballistic coefficient of approximately 357 kg/m^2, supports this observation, showing the largest difference in altitude history. In contrast, the Mars Human Mission vehicle has a mass of 100 metric tons, 100 times larger than that of the Moses Test Vehicle, but a ballistic coefficient of approximately 757 kg/m^2, slightly more than twice as large as that of the Moses Test Vehicle. The Mars Human Mission vehicle, with its relatively low ballistic coefficient with respect to its mass, also has the smallest overall variation in altitude history due to magnetohydrodynamic flow interaction.

B. Deceleration History: Influence of Magnetohydrodynamic Flow Interaction on Vehicle Deceleration

The deceleration vs. altitude profiles are presented below for both the unseeded and 1% K seeded cases for various entry vehicles and B field magnitudes as Figures 15 – 18.

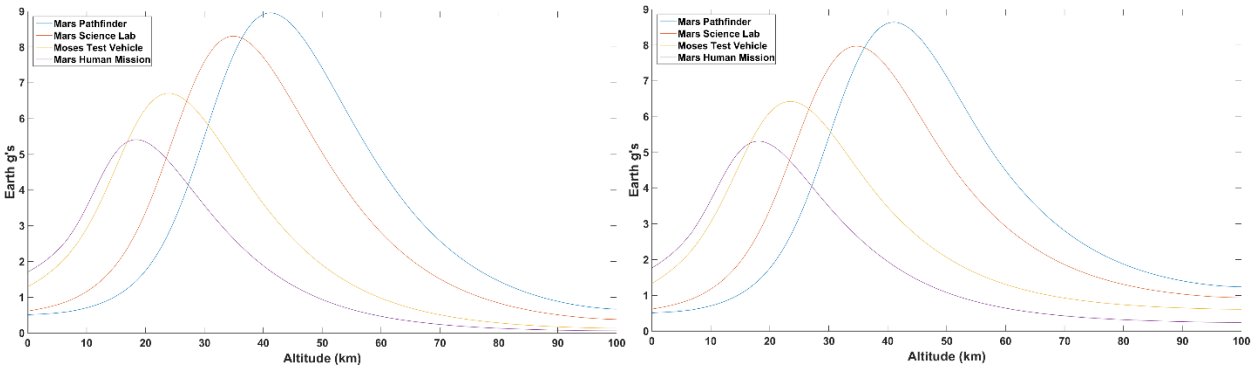

Figures 15 (Left) and 16 (Right). Deceleration vs. altitude for unseeded case with a 0.2T applied B field (left) and a 1.0T applied B-field (right).

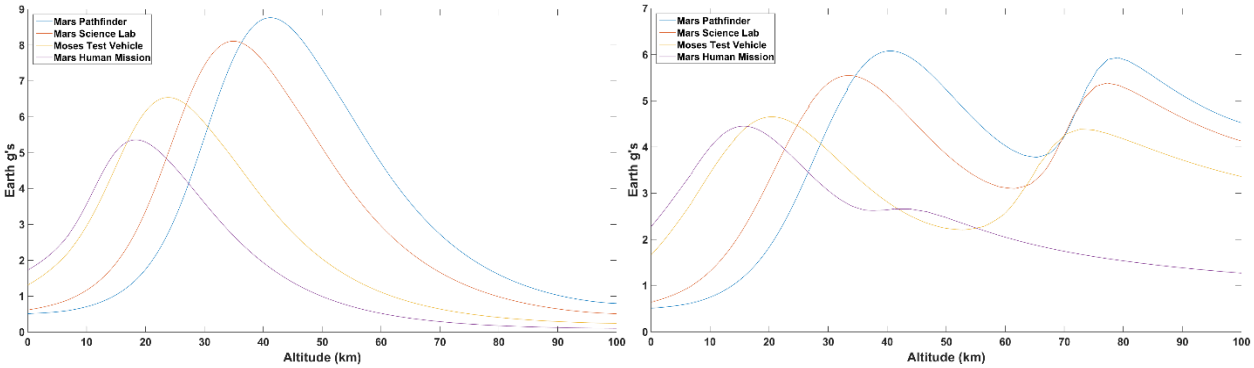

Figures 17 (Left) and 18 (Right). Deceleration vs. altitude for 1.0 % K seed case with a 0.2T applied B field (left) and a 1.0T applied B-field(right).

The results presented show that the influence of a 1.0 T applied B-field relative to that of a 0.2 T applied B-field is much more pronounced in the 1.0 % mass fraction K seeded case. In both cases, however, the higher imposed B-field reduced the peak deceleration and has a 'spreading' effect on the deceleration history. This effect is most apparent in Figure 18, where there exist two deceleration peaks: one dominated by magnetohydrodynamic flow interaction forces and the other dominated by aerodynamic forces. The results for the unseeded and 1% mass fraction K seed cases are presented numerically as Tables 5 and 6.

Table 5 Unseeded Case Peak Decelerations as a Function of B-field and Vehicle Configuration

Vehicle	Mars Pathfinder	Mars Science Lab	Moses Test Vehicle	Mars Human Mission
B Field	nMax Total (g's)	nMax Total (g's)	nMax Total (g's)	nMax Total (g's)
0 T	8.97	8.32	6.72	5.42
0.2 T	8.95	8.31	6.71	5.41
0.4 T	8.91	8.26	6.66	5.40
0.6 T	8.84	8.18	6.60	5.38
0.8 T	8.75	8.08	6.52	5.35
1.0 T	8.64	7.97	6.43	5.31
Ratio of 0T to 1.0T	1.04	1.04	1.05	1.02

Table 6 1% K Seeded Case Peak Decelerations as a Function of B-field and Vehicle Configuration

Vehicle	Mars Pathfinder	Mars Science Lab	Moses Test Vehicle	Mars Human Mission
B Field	nMax Total (g's)	nMax Total (g's)	nMax Total (g's)	nMax Total (g's)
0 T	8.97	8.32	6.72	5.42
0.2 T	8.76	8.11	6.54	5.36
0.4 T	8.20	7.54	6.07	5.20
0.6 T	7.44	6.79	5.48	4.96
0.8 T	6.70	6.09	5.00	4.69
1.0 T	6.08	5.55	4.65	4.45
Ratio of 0T to 1.0T	1.48	1.50	1.44	1.22

The numerical results in Tables 5 and 6 confirm the observations noted for figures 15 – 18. For the unseeded case shown in Table 5, there is a reduction in overall peak deceleration when applying a 1T magnetic field, but this reduction is only by a factor of 1.05. To contrast, in the 1% K seeded case shown in Table 6, this same reduction occurs at a factor of approximately 1.25 for the Mars Human Mission case, and 1.5 for the other three vehicle cases. The quantitative results for the maximum deceleration due solely to the magnetohydrodynamic flow interaction for the unseeded and 1% K seeded cases are presented below as Tables 7 and 8.

Table 7 Unseeded Case Peak MHD Decelerations as a Function of B-field and Vehicle Configuration

Vehicle	Mars Pathfinder	Mars Science Lab	Moses Test Vehicle	Mars Human Mission
B Field	nMax MHD (g's)	nMax MHD (g's)	nMax MHD (g's)	nMax MHD (g's)
0.2 T	0.02	0.02	0.02	0.01
0.4 T	0.10	0.09	0.08	0.03
0.6 T	0.21	0.21	0.19	0.07
0.8 T	0.38	0.37	0.32	0.13
1.0 T	0.60	0.58	0.50	0.20
Ratio of 1T to 0.2T	25.00	24.65	23.12	23.34

Table 8 1% K Seeded Case Peak MHD Decelerations as a Function of B-field and Vehicle Configuration

Vehicle	Mars Pathfinder	Mars Science Lab	Moses Test Vehicle	Mars Human Mission
B Field	nMax MHD (g's)	nMax MHD (g's)	nMax MHD (g's)	nMax MHD (g's)
0.2 T	0.21	0.21	0.19	0.08
0.4 T	0.83	0.83	0.76	0.30
0.6 T	1.82	1.81	1.63	0.67
0.8 T	3.13	3.08	2.74	1.15
1.0 T	4.75	4.65	4.09	1.72
Ratio of 1T to 0.2T	22.51	21.90	20.98	22.44

The peak magnetohydrodynamic flow interaction deceleration is approximately quadratic with B-field strength, and in the 1% K seeded case for the Mars Pathfinder, Mars Science Lab, and Moses Test Vehicles, greater than 50% of the peak deceleration without the applied magnetic field. In addition to this greater reduction in peak deceleration, the shape of the deceleration vs. altitude curve in Figure 18 is also significantly altered, seeing magnetohydrodynamic flow interaction dominated decelerations at much higher altitudes than normally seen for purely aerodynamic deceleration. This result could prove interesting for vehicle attitude control and peak heat transfer applications in future work.

V. Summary and Conclusions

A systems analysis capability for the effect of magnetohydrodynamic flow interaction on a planetary entry vehicle equipped with a magnetohydrodynamic energy generation system has been developed. The analysis techniques employed and the associated results demonstrate that magnetohydrodynamic flow interaction effects can be computed for a variety of entry vehicles using fundamental functional relationships between flow properties. The results show that magnetohydrodynamic flow interaction for the magnetic field configuration presented causes a significant increase in overall entry vehicle deceleration and trajectory given appropriate alkali metal seed and magnetic field strength. The effect of the flow interaction is similar to a decrease in the ballistic coefficient of a particular vehicle, essentially causing the vehicle to decelerate higher in the atmosphere. Consideration of active control of the magnetic field orientation and magnitude for inducing lift and moments on the vehicle is left to future work. This aspect of the magnetohydrodynamic flow interaction could prove particularly interesting due to the tendency of the majority of the additional drag to occur at much higher altitudes than the aerodynamic drag. To conclude, magnetohydrodynamic energy generation and flow control has the potential to significantly alter entry vehicle flight dynamics and should continue to be investigated for future Mars planetary entry system development.

Acknowledgments

This work is funded through a NASA Space Technology Research Fellowship, grant number NNX13AL82H. In addition, the authors would like to thank Dr. Robert Moses of NASA Langley research center for his advice towards the completion of this work.

References

[1] R. D. Braun, "Mars Exploration Entry , Descent and Landing Challenges," in *IEEE Aerospace Conference*, 2006.

[2] D. A. Spencer, R. C. Blanchard, R. D. Braun, P. H. Kallemeyn, and S. W. Thurman, "Mars Pathfinder Entry, Descent, and Landing Reconstruction," *J. Spacecr. Rockets*, vol. 36, no. 3, pp. 357–366, 1999.

[3] R. W. Moses, C. A. Kuhl, and J. D. Templeton, "Plasma Assisted ISRU At Mars," in *15th International Conference on MHD Energy Conversion*, 2005, p. 11.

[4] W. B. Bush, "A Note on Magnetohydrodynamic-Hypersonic Flow Past a Blunt Body," *Journal of the Aerospace Sciences*, vol. 26, no. 8. pp. 536–537, 1959.

[5] P. O. Jarvinen, "On The Use of Magnetohydrodynamics During High Speed Re-Entry," Everett, Massachusetts, 1964.

[6] S. Kranc, A. B. Cambel, and R. W. Porter, "Electrodeless Magnetogasdynamic Power During Entry," *J. Spacecr.*, vol. 4, no. 6, pp. 813–815, 1967.

[7] J. Poggie and D. V. Gaitonde, "Magnetic control of flow past a blunt body: Numerical validation and exploration," *Phys. Fluids*, vol. 14, no. 5, pp. 1720–1731, 2002.

[8] T. Fujino, T. Yoshino, and M. Ishikawa, "Numerical Analysis of Reentry Trajectory Coupled with Magnetohydrodynamics Flow Control," *J. Spacecr. Rockets*, vol. 45, no. 5, pp. 911–920, 2008.

[9] S. O. Macheret, M. N. Shneider, and G. V Candler, "Magnetohydrodynamic Energy Generation for Planetary Entry Vehicles," in *35th AIAA Plasmadynamics and Lasers Conference*, 2004.

[10] M. Kim and I. D. Boyd, "Effectiveness of a Magnetohydrodynamics System for Mars Entry," *J. Spacecr. Rockets*, vol. 49, no. 6, pp. 1141–1149, 2012.

[11] R. W. Ziemer and W. B. Bush, "Magnetic Field Effects on Bow Shock Stand-Off Distance," *Phys. Rev. Lett.*, vol. 1, no. 2, pp. 58–59, 1958.

[12] A. Gülhan, B. Esser, U. Koch, F. Siebe, J. Riehmer, D. Giordano, and D. Konigorski, "Experimental Verification of Heat-Flux Mitigation by Electromagnetic Fields in Partially-Ionized-Argon Flows," *J. Spacecr. Rockets*, vol. 46, no. 2, pp. 274–283, 2009.

[13] K. R. Lobb, "Experimental Measurement of Shock Detachment Distance on Spheres Fired in Air at Hypervelocities," *High Temp. Asp. Hypersonic Flows*, vol. 14, no. 5, pp. 519–527, 1964.

[14] P. R. Mahaffy, C. R. Webster, and E. Al., "Abundance and Isotopic Composition of Gases in the Martian Atmosphere from the Curiosity Rover," *Science (80-.).*, vol. 341, no. 6143, pp. 263–266, 2013.

[15] S. Gordon and B. J. McBride, "Computer Program for Calculation of Complex Chemical Equilibrium Compositions and Applications," *NASA Ref. Publ. 1311*, 1994.